Transient Freezing of Molten Salt in Pipes: A Multi-Scale CFD and Lumped-Parameter Model Analysis*

Hongxiang Yu,[1,2] Chong Zhou,[1,2,†] Yao Fu,[1,2] Shangwu Wang,[1] Yi-ang Yang,[1] Shuaiyu Xue,[1] and Hui Deng[1,2]

[1]*Shanghai Institute of Applied Physics, Chinese Academy of Sciences, Shanghai 201800, China*
[2]*University of Chinese Academy of Sciences, Beijing 100049, China*

Molten salts are efficient heat-transfer and storage media widely used in advanced energy systems, including nuclear and concentrated solar power. Their high melting points, however, can induce transient pipeline freezing, impairing operational economy and compromising flow safety. This study employs an integrated multiscale CFD and lumped-parameter approach to systematically investigate the complex freezing process of molten salt in pipes and to quantify the effect of key boundary conditions. Under pumped-inlet conditions, the characteristic temperature and flow rate exhibit a distinct dynamic: an initial decrease, followed by recovery and stabilization, marking the transition from initial filling to steady flow. Excessively designed cooling systems can drive the heat removal rate beyond a safe threshold. The risk of pipe blockage rises substantially for values of the dimensionless freezing parameter $\theta \leq 1$. The model's applicability is examined, and a parametric sensitivity analysis assesses the influence of inlet temperature, flow velocity, cooling intensity, pipe length, and wall thickness. This work provides a theoretical basis and safety-design guidelines for freeze-protection in molten salt cooling systems.

Keywords: Molten salt, Solidification/melting, Computational fluid dynamics (CFD), Cooling system design

I. INTRODUCTION

Molten salts are favored in advanced nuclear systems for their exceptional chemical stability and thermophysical performance at elevated temperatures [1], serving as primary heat-transfer and coolant media. As a cornerstone technology for Generation-IV nuclear reactors, molten salts enable transformative concepts such as the thorium fuel cycle and high-temperature process heat applications, offering a path toward sustainable and versatile nuclear energy [2–5]. In liquid-fueled molten salt reactors, they act as a solvent for nuclear fuel [6, 7], while in solid-fueled designs they function as the core coolant [8]. This dual role underscores their unique integration into reactor physics and thermal-hydraulic design [9]. A defining characteristic of these salts, however, is their high solidification point. Although this permits system operation at atmospheric pressure, it concurrently introduces a substantial risk of flow blockage due to freezing during operational transients, such as startup, shutdown, and under postulated accident conditions [10]. Unlike water-cooled systems where freezing is rarely a concern under operating conditions, the freezing point of molten salts lies within the operational temperature window, making transient thermal management a critical and ever-present design challenge [11, 12]. Effectively mitigating this freezing risk is therefore a central challenge for ensuring system safety and reliability.

The integrity of coolant flow is a fundamental safety requirement for molten salt reactors. Research dating back to Yamamoto's 1971 study on partial loop blockages underscores the imperative of maintaining unimpeded flow channels [13]. Consequently, engineering designs universally incorporate pipe insulation alongside active heating systems, typically electrical trace heating, to prevent freezing [14]. These measures are considered the first line of defense, designed to maintain the entire primary circuit above the liquidus temperature during normal and most off-normal operations [15]. Despite these precautions, safety analyses for design-basis events including station blackout (SBO) or heater failure demonstrate that local solidification upon contact with colder structures remains plausible [16, 17]. This is because the heat loss through insulation is non-zero, and during extended transients or accidents, the balance between heat generation, heat loss, and auxiliary heating can be disrupted. This risk is accentuated during transient phases like initial system filling, cooldown, or passive decay heat removal. It is particularly acute in fully passive safety systems such as the Direct Reactor Auxiliary Cooling System (DRACS) [18], which depends entirely on buoyancy-driven natural circulation. In a DRACS, heat is rejected to the ultimate heat sink through a natural circulation loop that must be initiated and sustained purely by density gradients. The system's success is predicated on a delicate balance [19, 20]. The modest driving force in such systems is exquisitely sensitive to flow resistance. An excessively efficient heat exchanger can induce rapid cooling of the salt, potentially initiating localized freezing. Even a partial occlusion in a pipe or the heat exchanger tube can dramatically increase the loop flow resistance [21]. This can disrupt the critical equilibrium between the buoyancy drive and flow resistance, leading to a loss of decay heat removal capability. Hence, quantifying a definitive thermal safety boundary to prevent overcooling is of paramount importance for reactor design. This boundary defines the minimum allowable salt temperature or the maximum allowable heat exchanger effectiveness for a given design to ensure freezing is precluded.

Accurately defining this boundary requires a mechanistic understanding of the transient solidification process un-

* This work was financially supported by the Shanghai Institute of Applied Physics, Chinese Academy of Sciences, through the State Key Laboratory of Thorium Energy (Grant No. SYS-ZBS-202403) and the Young Potential Program (Grant No. SINAP-YXJH-202411)
† Corresponding author, zhouchong@sinap.ac.cn

der flow conditions. This process constitutes a multiphysics problem, coupling multiphase flow, phase-change heat transfer, and porous media dynamics within a three-dimensional, unsteady framework. The solid-liquid mixture, known as the mushy zone, exhibits a complex, evolving structure that dictates both the heat transfer and hydraulic resistance [22–25]. Early investigations, exemplified by the experimental work of Pacheco et al. on solar salt systems, provided valuable macroscopic observations of freezing but lacked resolution of local, transient phenomena [26]. Such integral experiments were crucial for identifying gross parameters like total frozen mass but could not resolve the internal morphology of the freeze front or the local velocity fields within the slushy region. While system-level codes are indispensable for integral safety analysis [27], they possess inherent limitations in capturing the localized, flow-dependent details of freeze-front propagation. Computational Fluid Dynamics (CFD) has emerged as an indispensable tool for elucidating these micro-scale mechanisms. CFD simulations enable detailed resolution of the solidification front evolution, flow channel occlusion within the mushy zone, and the consequent effects on system pressure drop and thermal hydraulics. For example, Lu et al. employed ANSYS Fluent simulations of a cold-fill scenario to derive a critical inlet temperature threshold for blockage prevention [28]. Subsequent studies have leveraged CFD to quantify the sensitivity of the freezing process to key parameters (e.g., the mushy zone constant) and to calibrate models against experimental data, thereby significantly enhancing predictive fidelity and validating CFD's critical role in fundamental research [29].

Nevertheless, the considerable computational expense of high-fidelity 3D CFD simulations precludes their direct use for rapid design iteration or real-time safety margin evaluation. A single high-resolution transient simulation of a freezing event in a representative geometry can require days of computational time on high-performance clusters, making parametric studies and extensive sensitivity analyses prohibitively costly [30, 31]. This creates a compelling need for a rapid, physics-informed prediction methodology that retains essential mechanistic accuracy while offering computational efficiency, thereby bridging the gap between detailed simulation and engineering application. Ideal tools for this purpose are reduced-order models or analytical criteria derived from first principles and informed by high-fidelity simulation insights [32, 33]. They should encapsulate the dominant physics into a simplified formulation that can be evaluated nearly instantaneously. Foundational work in analogous areas, such as the solidification risk model for lead-bismuth eutectic systems developed by Zeng et al., provides a valuable methodological reference [34]. Their approach successfully distilled system program results into a practical correlation for predicting blockage, demonstrating the feasibility and utility of such a methodology. Building directly upon this paradigm, the present study seeks to address the identified gap for molten salt systems. Informed by insights gleaned from high-fidelity CFD, this work aims to develop a rapid freezing criterion and an associated framework for predicting safety boundaries. The objective is to formulate a physics-informed, simplified tool that balances mechanistic rigor with computational practicality. This approach is intended to support the design and safety analysis of molten salt reactor coolant systems, with particular relevance to passive safety architectures. It is hoped that this work will contribute usefully to the methodology for assessing freezing risk, thereby supporting the advancement of inherently safe nuclear energy technology.

The paper is organized as follows. Section II details the numerical methodology, including the CFD model and its validation against experimental data. Section III presents simulation results, categorizes freezing scenarios, and analyzes the blockage development process. Section IV derives an engineering-oriented freeze-plugging criterion from fundamental energy principles, discusses its domain of applicability, and performs a comprehensive parametric sensitivity study. Concluding remarks are provided in Section V.

II. NUMERICAL METHODOLOGY

A. Physical Model

As depicted in Fig. 1a, a three-dimensional geometric model of molten salt filling a cold pipe is constructed based on a Cartesian coordinate system. The model incorporates a fluid domain and a solid domain of specified thickness. The geometry is configured with reference to conventional pipe applicated in the design of salt/air heat exchangers in the DRACS. The horizontal steel pipe, featuring an inner radius $R_1 = 0.005\,\mathrm{m}$ and an outer radius $R_2 = 0.006\,\mathrm{m}$, comprises an inlet section and a cold section with lengths $L_{in} = 0.2\,\mathrm{m}$ and $L_c = 1\,\mathrm{m}$, respectively. The pressure difference at the pipeline inlet and outlet is P_0. At $t = 0$, the molten salt initiates the filling process with an initial temperature T_0, the temperature of the inlet section is equal to T_0 and the temperature of the cold section T_p is below the melting point of the molten salt. The outer wall temperature of the inlet section is maintained at the molten salt's initial temperature T_0 and the heat transfer coefficient outside the cold section is h_0 with the surrounding temperature T_∞. It should be noted that in all simulations, both the surrounding temperature and the initial temperature of the cold pipe are set to 300 K.

The simulation employs KNO_3-$NaNO_2$-$NaNO_3$ (Hitec, 53-40-7 wt%) molten salt. The thermophysical properties of the molten salt [35] are listed as follows: $\rho_m = 2293 - 0.7497T\ \mathrm{kg\,m^{-3}}$, $c_m = 5806 - 10.833T + 7.2413 \times 10^{-3}T^2\ \mathrm{J\,kg^{-1}\,K^{-1}}$, $\lambda_m = 0.78 - 1.25 \times 10^{-3}T + 1.6 \times 10^{-6}T^2\ \mathrm{kg\,m^{-1}\,s^{-1}}$, $\mu_m = 0.4737 - 2.297 \times 10^{-3}T + 3.371 \times 10^{-6}T^2 - 2.019 \times 10^{-9}T^3\ \mathrm{kg\,m^{-1}\,s^{-1}}$, Among them, the unit of T is K. The study by Zhang et al. [35] provides a key reference for the thermal properties related to solidification, $Q = 80000\ \mathrm{J\,kg^{-1}}$, $T_s = 406.5$ K, $T_l = 418.2$ K. The surface tension between molten salt and air $\sigma = 0.149 - 0.0000556T\ \mathrm{N\,m^{-1}}$ [1]. Gravity acceleration g is $9.81\,\mathrm{m\,s^{-2}}$. The thermophysical properties of air and steel, with reference temperature at surrounding temperature (approximately 300 K), can be obtained from the reference [36]: $\rho_{st} = 8030\ \mathrm{kg\,m^{-3}}$, c_{st}

= 502.48 $\mathrm{J\,kg^{-1}\,K^{-1}}$, λ_{st} = 16.27 $\mathrm{kg\,m^{-1}\,s^{-1}}$; ρ_a = 1.225 $\mathrm{kg\,m^{-3}}$, c_a = 1006.43 $\mathrm{J\,kg^{-1}\,K^{-1}}$, λ_a = 0.0242 $\mathrm{kg\,m^{-1}\,s^{-1}}$, μ_a = 0.000017894 $\mathrm{kg\,m^{-1}\,s^{-1}}$.

B. Governing Equations

The entire filling process involves multiphase flow and is simulated using the Volume of Fluid method [37, 38]. This approach tracks the interface between phases by solving the volume fractions of different phases, constrained as follows:

$$\alpha_m + \alpha_a = 1 \tag{1}$$

where α_m and α_a denote the volume fractions of molten salt and air, respectively. The momentum and energy equations are shared among the phases, with material properties determined by the volume-weighted average of each phase:

$$x = \alpha_m x_m + \alpha_a x_a \tag{2}$$

where x represents density (ρ), specific heat capacity (c), thermal conductivity (λ), or dynamic viscosity (μ).

During the molten salt filling process, solidification and melting phenomena occur. The enthalpy-porosity technique is employed to simulate these phase changes [39, 40] melt interface tracking methods, this technique calculates the liquid fraction through enthalpy balance. The mushy zone is a region in which the liquid fraction lies between 0 and 1. The mushy zone is modeled as a "pseudo" porous medium in which the porosity decreases from 1 to 0 as the material solidifies.

The total enthalpy H of the fluid is the sum of sensible enthalpy h_{sen} and latent heat ΔH:

$$H = h_{sen} + \Delta H \tag{3}$$

The sensible enthalpy h_{sen} is the product of the specific heat and temperature which can be written as:

$$h_{sen} = c_m T \tag{4}$$

where c_m is the specific heat capacity of molten salt.

The liquid fraction f_l is expressed as:

$$f_l = \begin{cases} 0, & T < T_s \\ \dfrac{T - T_s}{T_l - T_s}, & T_s < T < T_l \\ 1, & T > T_l \end{cases} \tag{5}$$

the region where f_l ranges from 0 to 1 is termed the mushy zone, a semi-solid region in which the porosity decreases from 1 to 0 as the material solidifies.

The latent heat ΔH is calculated as the product of the liquid fraction f_l and the latent heat of fusion Q:

$$\Delta H = f_l Q \tag{6}$$

The energy equation is formulated as [41]:

$$\frac{\partial}{\partial t}(\rho H) + \nabla \cdot (\rho \vec{v} H) = \nabla \cdot (\lambda \nabla T) + S \tag{7}$$

where the phase related source S is:

$$S = \frac{\partial}{\partial t}(\rho \Delta H) + \nabla \cdot (\rho \vec{v} \Delta H) \tag{8}$$

The momentum equation is given by:

$$\frac{\partial}{\partial t}(\rho \vec{v}) + \nabla \cdot (\rho \vec{v} \vec{v}) = -\nabla P + \nabla \cdot \left[\mu(\nabla \vec{v} + \nabla \vec{v}^T)\right] + \rho \vec{g} + A \tag{9}$$

Here, $\vec{g}$ represents gravitational acceleration vector. A is the momentum sink term due to solidification expressed by the Carman-Kozeny equation, a well-known equation derived from the Darcy law [42]:

$$A = \frac{(1 - f_l)^2}{(f_l^2 + \varepsilon)} A_{mush} \vec{v} \tag{10}$$

where ε is a small constant (0.001) to prevent division by zero. Within the mushy zone, as the fluid solidifies, f_l decreases from 1 to 0, and the velocity approaches zero. The mushy zone constant A_{mush} controls the rate of velocity reduction during solidification; a higher value results in a more rapid decrease in velocity.

The governing equation in the steel pipe is:

$$c_{st} \frac{\partial T}{\partial t} = \lambda_{st} \nabla^2 T \tag{11}$$

C. Simulation Procedure and Model Verification

The simulations were performed using the commercial software ANSYS FLUENT. The computational domain was discretized with finite volume grids, with all variables stored and calculated at the cell centers. A laminar flow model was applied. To enhance stability in simulating the complex transient processes, the pressure-velocity coupling was resolved using the PISO algorithm, and the PRESTO scheme was employed for pressure interpolation. Furthermore, a double-precision solver was utilized for solving the momentum and energy equations to improve the accuracy of the transient calculations.

A three-dimensional filling geometry model was established. To increase the stability of transient calculations, the mesh division was fully hexahedral structured. Considering

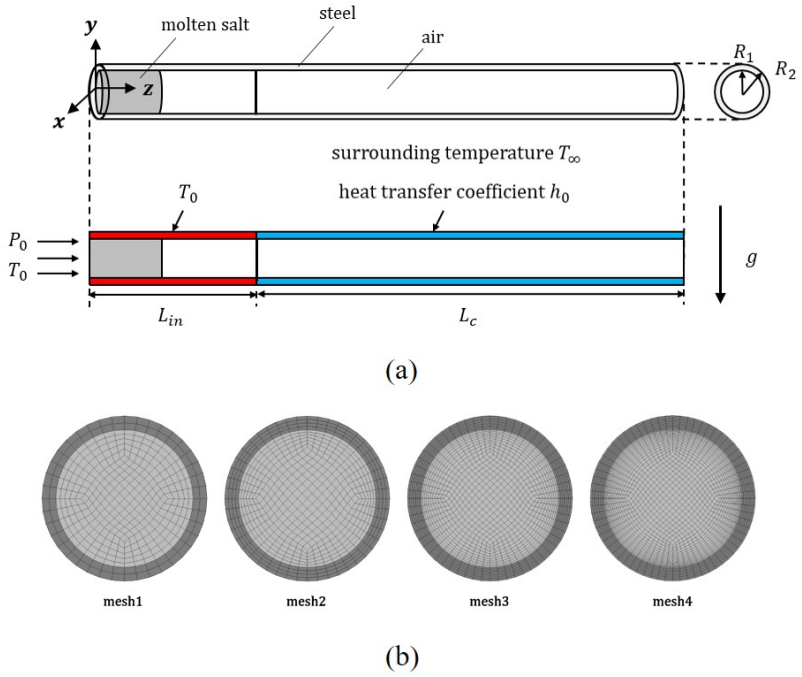

Fig. 1. Schematic view of (a) simulation geometry,boundary conditions and (b) mesh schemes.

the solidification layer growth near the cold wall, the near-wall mesh was continuously refined, as shown in Fig. 1b. Four schemes were tested for mesh independence validation. The growth of the solidified layer brings additional flow resistance, affecting the transient flow process. The simulation results show that when the near-wall mesh thickness is refined to above $0.1\,\mathrm{mm}$, the rate of change of flow distance over time is less than 5%. The global liquid fraction calculation results under different mesh schemes differed by less than 3%. Finally, mesh3 was selected, its main flow domain element size was $0.5\,\mathrm{mm}$, near-wall zone element size was $0.1\,\mathrm{mm}$, total grid number was 460800. The time step $\Delta t = 0.001\,\mathrm{s}$ was chosen, its related liquid fraction calculation results differed by less than 1% compared with $\Delta t = 0.0005\,\mathrm{s}$.

The solid-liquid phase change was simulated using the enthalpy-porosity model which accounts for the latent heat and introduces a momentum damping effect within the mushy zone. The damping intensity is governed by the material-dependent mushy zone constant, A_{mush}. To calibrate this key parameter, the numerical model was verified against the experimental data of Zhang et al. [35]. Fig. 2 compares the simulated penetration distances across a range of A_{mush} values with the experimental measurements. For Hitec salt, an A_{mush} value of 5×10^4 yielded the optimal agreement. This good correspondence verifies the reliability of the present computational methodology for subsequent studies.

With an appropriate mushy zone constant obtained for Hitec, the trend of solidification induced additional flow resistance is well captured. A further discussion on the rationality of the inlet boundary condition is necessary, both for the initial filling and for steady state flow. In a real system, the hydraulic head (e.g., from a pump or pneumatic pressure) is distributed across components with limited capacity. When solidification occurs, the resulting resistance perturbation disrupts the flow regime. For such extreme conditions, temperature, pressure, and velocity are strongly coupled: a drop below the critical temperature triggers solidification, causing a sudden resistance rise that reduces or even stops the flow. Therefore, a pressure dependent inlet boundary condition that allows backflow is essential to reasonably simulate the transient dynamic behavior during solidification.

During the initial filling stage of the molten salt, the pipe contains only air, and the density difference between molten salt and air is substantial. Consequently, the pressure loss due to the molten salt flow dominates, while the influence of the air can be reasonably neglected. In the boundary condition settings, the outlet pressure is set to 0. Therefore, at t = 0, the prescribed total pressure difference is entirely converted into the dynamic pressure of the molten salt, i.e., ΔP = P_0 = $\rho u_0^2/2$. Hence, the initial velocity of the molten salt can be directly calculated from the given inlet pressure.

III. NUMERICAL RESULTS AND ANALYSIS

The analysis in Section III focuses on the transient freezing of molten salt as it flows into a cold pipe. This process is governed by a critical positive feedback loop: the growth of a solid layer adjacent to the pipe wall increases the flow resistance, which reduces the flow rate and in turn accelerates further solidification, potentially culminating in complete flow blockage. To accurately simulate this coupled transient phe-

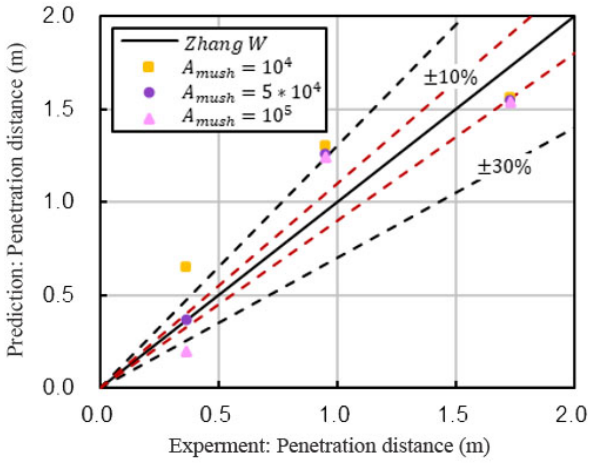

Fig. 2. Comparison of penetration distances between the experimental data and the simulation results.

nomenon, a pressure boundary condition that reflects actual pump characteristics is essential. This methodology is consistent with the approach of Lu et al. [28] and supported by Yu et al. [29] in their discussions on boundary condition assumptions for practical engineering scenarios.

A. Characteristics of Pressure-Driven Flow Regimes in Cold Pipe

Fig. 3a illustrates the typical progression of a cold-pipe filling process, which transitions from the initial filling stage to the establishment of thermal equilibrium under sustained flow. The temporal evolution of key parameters under different inlet pressures, P_0, is detailed in Fig. 3b-e. Here, the characteristic temperature is defined as the average temperature at the advancing flow front, representing the minimum streamwise temperature; upon complete filling, it becomes equivalent to the average outlet temperature. And the wall temperature and the wall heat flux represent spatial averages along the entire cold pipe section. At $t = 0$, the prescribed total pressure difference is entirely converted into the dynamic pressure of the molten salt. Once the molten salt starts flowing into the pipe, the total pressure is gradually consumed by the frictional losses along the pipe, resulting in a rapid decay of the mass flow rate. The corresponding initial mass flow rates of molten salt for P_0 = 108, 224, 458, and 860 Pa are 0.051, 0.074, 0.11, and 0.14 $\mathrm{kg\,m^{-1}}$, respectively.

The general trends observed across different pressure conditions are similar. For the case with $P_0 = 860\,\mathrm{Pa}$, shown in Fig. 3b-e, the initial constant pressure difference is entirely converted into kinetic energy, driving molten salt into the empty pipe at a high initial flow rate. As filling progresses, the salt is cooled by the cold pipe wall. This results in a significant heat flux, causing the characteristic temperature to decrease while simultaneously heating the pipe wall. Concurrently, increasing flow resistance leads to a rapid decay in the mass flow rate. Once the molten salt front reaches the outlet, the continuous inflow of molten salt raises the characteristic temperature. The associated reduction in fluid viscosity lowers the frictional resistance, allowing the mass flow rate to recover. After approximately 30 s, the pipe wall temperature stabilizes under the specified heat transfer conditions, establishing a steady thermal gradient as the flow reaches an equilibrium state.

A lower inlet pressure differential results in a lower initial flow rate. For $P_0 = 108\,\mathrm{Pa}$, a distinct behavior is observed when $16 < t < 30\,\mathrm{s}$, where the characteristic temperature within the one-meter pipe decreases to a level near the mushy zone. For the case P_0 = 108 Pa, the behavior is analogous to that presented in Fig. 4d: during the transition from initial filling to a more stable flow, the molten salt temperature falls into the mushy zone for a period. The effect of the initial air temperature is negligible due to the short filling time; the temperature reduction of the molten salt is primarily caused by heat transfer to the cold pipe wall. The local solidification that occurs introduces additional flow resistance, causing the flow rate to stagnate at a persistently low value. Despite this significant flow attenuation, the molten salt ultimately maintains through-flow, and the system progresses to a final state of combined thermal and hydraulic equilibrium.

B. Initial Filling Stage: Freezing Blockage During Initial Flow Establishment

The analysis in Section III.A indicates that an insufficient inlet pressure during the initial filling stage can readily induce freezing and blockage. This is conclusively demonstrated in Fig. 4a, where for $P_0 = 108\,\mathrm{Pa}$, a reduction in the inlet temperature by $50\,^{\circ}\mathrm{C}$ leads to complete freezing within the one-meter pipe. In contrast, Fig. 4c shows that increasing the inlet pressure by 750 Pa enables the molten salt to traverse the entire pipe length and achieve thermal equilibrium, even when the inlet temperature is reduced by $75\,^{\circ}\mathrm{C}$. These results underscore that an adequate pressure head constitutes the primary and essential barrier for ensuring safe heat removal during this phase.

While sufficient upstream driving force allows the fluid to successfully fill the empty pipe, an excessively low inlet temperature will cause the salt to cool to its freezing point too rapidly, resulting in blockage. Fig. 4b presents results for different inlet temperatures, ranging from 425 K to 445 K, under an inlet pressure $P_0 = 458\,\mathrm{Pa}$. Two distinct outcomes are identified: i) Complete freezing occurs at inlet temperatures $T_0 = 425$ K, 430 K, characterized by the characteristic temperature falling below the mushy zone and the flow rate decaying to zero. ii) Conversely, complete through-flow occurs at $T_0 = 435$ K, 445 K, where both parameters recover and stabilize. This identifies a critical inlet temperature for a given pipe geometry, below which freezing is inevitable during initial filling.

To provide clearer insight into the transient phase-change process, Fig. 4d-e presents a comparative visualization of liquid fraction contours for inlet temperatures of 425 K and 435

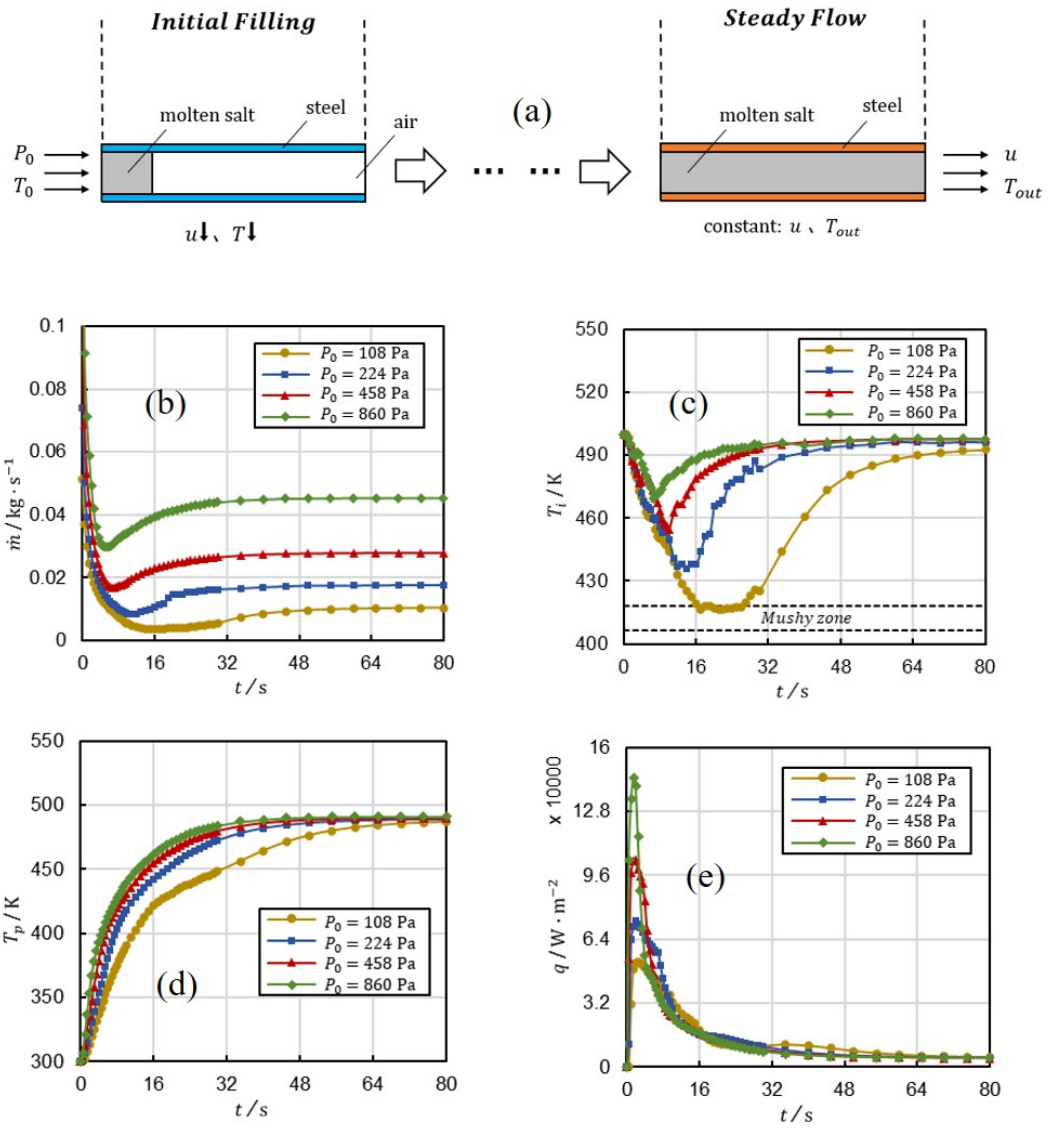

Fig. 3. The cold filling process: (a) schematic diagram and variation of characteristic quantities (T_0 = 500 K, h_0 = 20 W m^{-2} K^{-1}) (b) mass flow (c) characteristic temperature (d) wall temperature (e) wall heat flux.

K, respectively. These two cases, situated on opposite sides of the identified critical inlet temperature threshold, exemplify the fundamentally distinct freezing regimes and ultimate outcomes for the system.

In the sub-critical scenario ($T_0 = 425\,\mathrm{K}$), as seen in Fig. 4d, solidification initiates non-uniformly from the cold pipe wall due to local heat transfer variations. The solid phase, forming a mushy zone, grows radially inward in an accelerating manner. This acceleration occurs because the progressive occlusion of the flow channel reduces the advective heat transport from the warmer core fluid, thereby favoring further solidification growth. Consequently, the flow cross-section is progressively constricted until complete flow channel blockage is achieved, which corresponds to the flow decay and system failure observed in the macroscopic results.

Conversely, in the super-critical scenario ($T_0 = 435\,\mathrm{K}$), shown in Fig. 4e, the system exhibits a self-limiting behavior. Solidification similarly begins at the wall, but the higher inlet enthalpy provides a greater thermal inertia against freezing. Notably, under the influence of gravity, the denser, solid-rich phase segregates and concentrates at the bottom of the pipe, forming a distinct asymmetric layer, while the upper region remains largely clear for fluid passage. This bottom layer is then subjected to the continuous scouring and convective heat transfer from the incoming hotter bulk flow. A dynamic equilibrium is subsequently established where the rate of convective remelting at the interface of the solid layer balances the rate of conductive heat loss to the wall. After this transient period, the system stabilizes with a partially reduced but stable flow area, allowing for sustained operation without catastrophic blockage.

This direct visual comparison underscores the critical role

of inlet temperature in determining the fate of the system. It validates that maintaining the inlet condition above a specific threshold is essential to avoid the positive feedback loop that leads to complete occlusion and to ensure the system reaches a stable, safe thermal-hydraulic equilibrium.

C. Steady-State Stage: Critical Freezing Under Fully-Developed Flow

The analysis in this section extends the investigation to a fully developed, steady flow, examining the system's response when the cooling intensity exceeds a critical limit. This scenario is particularly pertinent for defining precise safety boundaries in the design of cooling systems intended for steady-state operation.

Fig. 5a-b presents the system's response to different heat transfer coefficients applied after the flow is largely stabilized beyond 80 s. A baseline coefficient of $20\,\mathrm{W\,m^{-2}\,K^{-1}}$ was used prior to this time. For a heat transfer coefficient $h_0 = 100\,\mathrm{W\,m^{-2}\,K^{-1}}$, shown in Fig. 5a, the characteristic temperature initially decreases and fluctuates near the mushy zone before eventually recovering. Correspondingly, the flow rate exhibits a distinct "concave profile" before returning to a stable value. In sharp contrast, for a coefficient $h_0 = 200\,\mathrm{W\,m^{-2}\,K^{-1}}$ shown in Fig. 5b, both the characteristic temperature and mass flow rate undergo an irreversible and precipitous decay. As the temperature drops definitively below the mushy zone, complete freezing occurs within the pipe.

The underlying spatial progression of these freezing processes is visualized in Fig. 5c-d, providing a direct spatial-temporal elucidation of how external cooling intensity dictates the system's thermal-hydraulic fate.

For the case with $h_0 = 100\,\mathrm{W\,m^{-2}\,K^{-1}}$, depicted in Fig. 5c, the enhanced cooling disrupts the established thermal balance shortly after its application. This perturbation triggers a self-limiting transient. Solidification initiates at the wall and, driven by gravity and natural convection within the mushy zone, accumulates predominantly at the pipe bottom ($80 < t < 180\,\mathrm{s}$). This results in the formation of a dense, stratified solid layer that partially constricts the flow area. Subsequently, heat from the sustained inflow gradually remelts this solidified layer, demonstrating a dynamic competition between external heat removal and internal convective heating. This process allows a new thermal equilibrium to be established ($180 < t < 300\,\mathrm{s}$), characterized by a stable, reduced flow cross-section that maintains continuous operation.

For the case with $h_0 = 200\,\mathrm{W\,m^{-2}\,K^{-1}}$, shown in Fig. 5d, the system crosses a stability threshold and enters an irreversible freezing trajectory. Solidification progresses more rapidly at the bottom. The swift growth and gravitational settling of the solid phase severely impede the flow, leading to a distinctive "air region" form near the top of the outlet, which is a clear hydrodynamic signature of near-complete lower path occlusion. The cooling intensity here critically overwhelms the flow's reheating capacity, creating a positive feedback loop where flow reduction further promotes freezing. This unarrested process reaches the critical condition for global solidification, resulting in complete blockage of the pipe by 300s.

The stark contrast between these two evolution sequences underscores a key mechanistic finding: the external cooling coefficient (h_0) acts as a decisive bifurcation parameter. Below a critical value, the system possesses sufficient thermal inertia and recovery capability to stabilize. Above it, the balance is irreversibly tipped towards runaway solidification and system failure. Fig. 5 thus visually validates the concept of a critical thermal safety boundary governed by cooling intensity.

IV. THEORETICAL MODEL AND DISCUSSION

To prevent heat transfer failure from molten salt freezing in cold pipes, previous studies have proposed several operational strategies. Yu et al. suggested using higher pump power to reduce the cooling duration [43]. A more conservative approach by Ben et al. advised maintaining the pipe wall temperature consistently above the salt's melting point [18]. To advance beyond these general guidelines and establish quantifiable safety boundaries for system design, this section develops thermal equilibrium equations to establish a freezing risk assessment criterion and enables a quantitative sensitivity analysis of key parameters.

A. Thermal Equilibrium Model Formulation

Section III established that freezing risk emerges when the characteristic temperature enters the mushy zone. A primary design objective is therefore to ensure the bulk outlet temperature remains above the liquidus temperature. Fig. 6a shows a schematic of a differential control volume for pipe flow. Here, dz and dt are infinitesimal length and time elements. The fluid temperature T is a function of axial distance z. The pipe inner and outer diameters are d_i and d_o.

An energy balance for the fluid control volume accounts for sensible and latent enthalpy changes:

$$\Delta h_{sen} + \Delta h_{lat} = -K(T(z) - T_\infty) \cdot \pi d_o \tag{12}$$

The left side is the fluid enthalpy drop. The right side represents heat dissipation to the environment at temperature T_∞. The coefficient K is the overall heat transfer coefficient, based conservatively on the outer pipe area:

$$K = 1/\left(\frac{1}{h_i}\frac{d_o}{d_i} + \frac{d_o}{2\lambda_s}\ln\frac{d_o}{d_i} + \frac{1}{h_o}\right) \tag{13}$$

Here, λ_s is the pipe thermal conductivity. The terms h_i and h_o are the convective heat transfer coefficients on the fluid-pipe and environment-pipe interfaces, respectively.

When the outlet temperature satisfies $T_{out} \geq T_l$, the enthalpy drop is dominated by sensible heat. And Eq. (12) simplifies to:

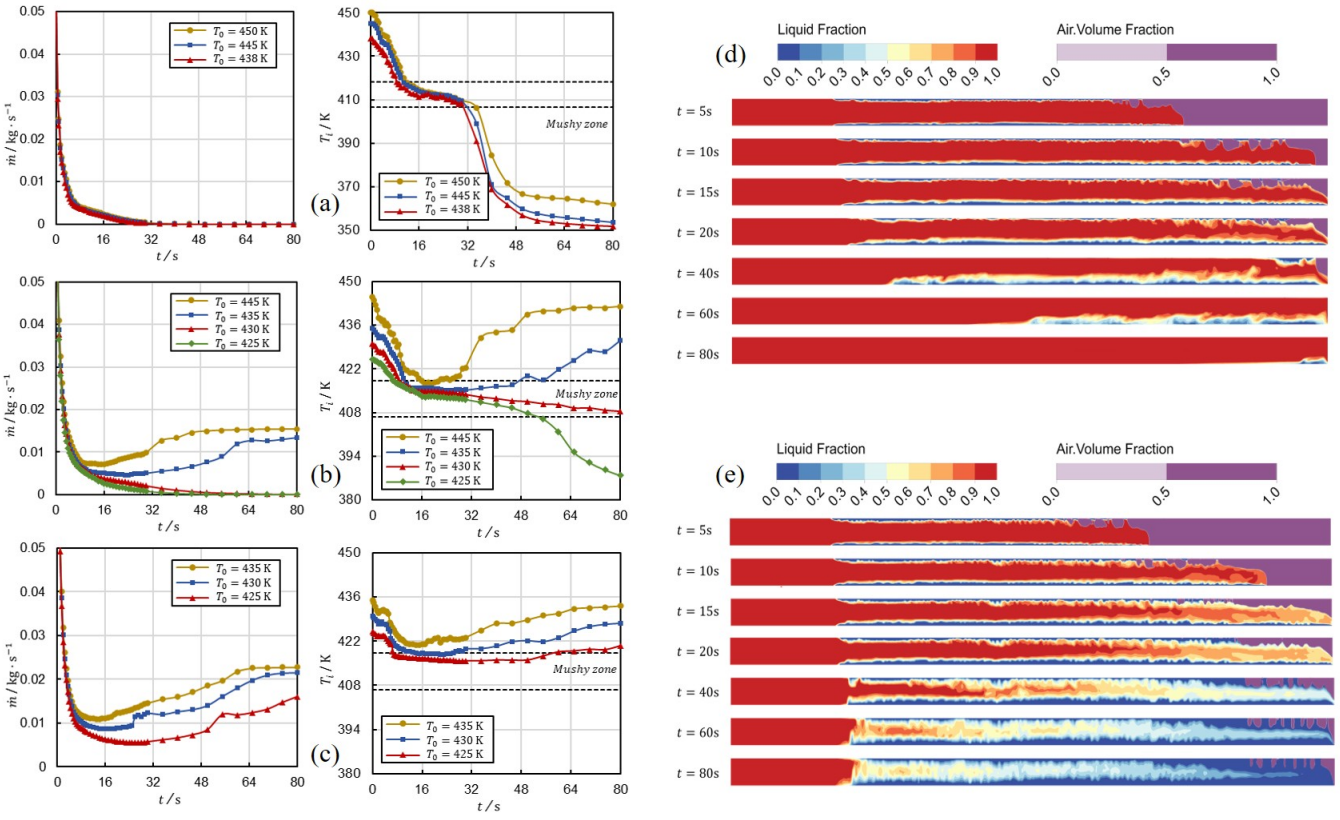

Fig. 4. Initial filling stage: variation of mass flow (left) and characteristic temperature (right) (a) $P_0 = 108\,\mathrm{Pa}$ (b) $P_0 = 458\,\mathrm{Pa}$ (c) $P_0 = 860\,\mathrm{Pa}$, and contours of liquid fraction ($P_0 = 458\,\mathrm{Pa}$, H:L = 5:1) (d) $T_0 = 435\,\mathrm{K}$ (e) $T_0 = 425\,\mathrm{K}$.

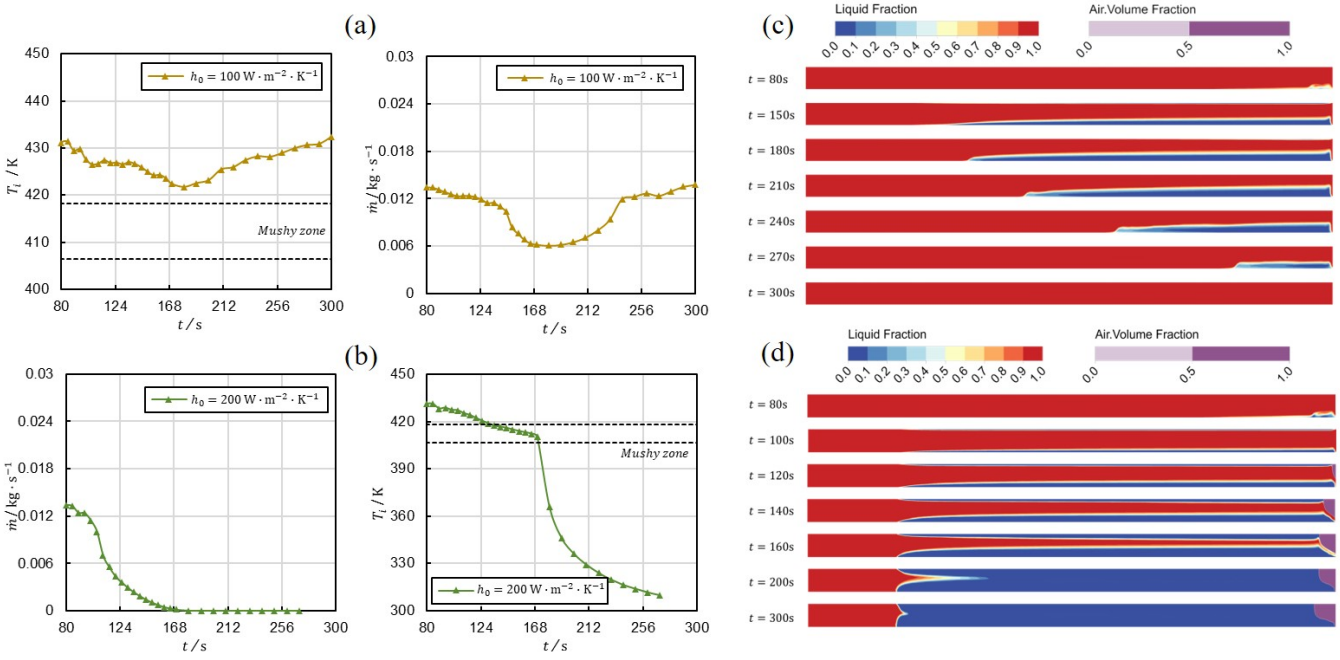

Fig. 5. Steady-state stage: variation of mass flow (left) and characteristic temperature (right) ($P_0 = 458\,\mathrm{Pa}$, $T_0 = 435\,\mathrm{K}$) (a) $h_0 = 100\,\mathrm{W\,m^{-2}\,K^{-1}}$ (b) $h_0 = 200\,\mathrm{W\,m^{-2}\,K^{-1}}$, and contours of liquid fraction (H:L = 5:1) (c) $h_0 = 100\,\mathrm{W\,m^{-2}\,K^{-1}}$ (d) $h_0 = 200\,\mathrm{W\,m^{-2}\,K^{-1}}$.

$$\frac{1}{4}\pi d_o^2 \cdot \rho_l u c_l \left(\frac{dT(z)}{dz}\right) = -K(T(z) - T_\infty) \cdot \pi d_o \quad (14)$$

Here ρ_l and c_l are the fluid density and specific heat. The

velocity $u = dz/dt$.

Rearranging Eq. (14) gives:

$$dT/dz + \frac{4K}{\rho_l u c_l d_o} T(z) = \frac{4KT_\infty}{\rho_l u c_l d_o} \tag{15}$$

The fluid temperature $T(z)$ is subject to these boundary conditions:

$$\lim_{z\to 0} T(z) = T_0 \tag{16}$$

$$\lim_{z\to \infty} T(z) = T_\infty \tag{17}$$

Solving Eq. (15) with conditions (16) and (17) yields:

$$T = T_\infty + (T_0 - T_\infty) e^{-\frac{4K}{\rho_l u c_l d_o} z} \tag{18}$$

This solution shows an exponential temperature decay along the pipe. Eq. (18) describes steady, fully-developed flow. For the short initial cold-filling process, assuming constant wall temperature ($K = h_i$, $T_\infty = T_w$) makes Eq. (18) consistent with the criterion from Zeng et al [34].

When the fluid is in the mushy zone ($T_s < T_{out} < T_l$), latent heat dominates. Following the approach of Voller et al. [40], Eq. (12) becomes:

$$\frac{1}{4}\pi d_o^2 \cdot \rho_l u_m \frac{Q}{T_l - T_s} \frac{dT(z)}{dz} = -K(T(z) - T_\infty) \cdot \pi d_o \tag{19}$$

u_m denotes the constant molten salt superficial velocity in the mushy zone. The corresponding boundary conditions are:

$$\lim_{z\to z_l} T(z) = T_l \tag{20}$$

$$\lim_{z\to \infty} T(z) = T_\infty \tag{21}$$

The solution is:

$$T = T_\infty + (T_l - T_\infty) e^{-\frac{4K(T_l - T_s)}{\rho_l u_m d_o Q}(z - z_l)} \tag{22}$$

Within the mushy zone, velocity decays linearly:

$$u_m = \begin{cases} 0, & T < T_s \\ \dfrac{T - T_s}{T_l - T_s} \cdot u, & T_s < T < T_l \\ u, & T > T_l \end{cases} \tag{23}$$

Liquid fraction follows a similar relation:

$$f_l = \begin{cases} 0, & T < T_s \\ \dfrac{T - T_s}{T_l - T_s}, & T_s < T < T_l \\ 1, & T > T_l \end{cases} \tag{24}$$

For a horizontal straight pipe, when the fluid temperature is above T_l, the total pressure drop is purely frictional: $\Delta P = \Delta P_f$. When the temperature falls into the mushy zone, this region is treated as a pseudo porous medium. The fluid still possesses its original properties, but an additional loss is introduced. The total pressure drop then consists of frictional loss and an additional loss, with the additional loss being dominant, as expressed in Eqs. (25):

$$\Delta P = \Delta P_f + \Delta P_e = f \cdot \frac{z}{D} \cdot \frac{\rho u_m^2}{2} + A_{mush} \cdot \frac{(1 - f_l)^2}{(f_l^2 + \varepsilon)} \cdot u_m \tag{25}$$

Eqs. (18) through (25) form the governing system for steady-state pipe flow and heat transfer. According to Eqs. (23), inside the mushy zone, the initial temperature of the molten salt corresponds to a velocity $u_m = u$. For the next time step (or next axial position z), the velocity is updated as $u_m = u(T - T_s)/(T_l - T_s)$, respectively. This allows a stepwise representation of temperature variation along the pipe. To validate the model and elucidate the underlying physics, it is applied to a representative case of Hitec salt flow with the characteristic parameters $T_0 = 580\,\mathrm{K}$, $u = 0.05\,\mathrm{m\,s^{-1}}$ and $T_\infty = 300\,\mathrm{K}$, yielding the pivotal results synthesized in Fig. 6b-c.

The thermal behavior is captured in Fig. 6b. The simulated temperature profile exhibits a nearly linear decrease over the initial pipe segment. This observed linearity is not contradictory to, but rather a specific manifestation of, the exponential decay form governed by Equations Eqs. (18) and Eqs. (22)—within a short development length, the leading-order term of the expansion dominates, presenting a quasi-linear trend. A key thermodynamic transition occurs as the temperature descends into the phase-change interval. Here, the release of latent heat within the mushy zone acts as a distributed internal heat source, absorbing a substantial portion of the sensible thermal energy and thereby markedly attenuating the local cooling rate, causing a distinct deviation from the initial linear slope.

The corresponding hydrodynamic response, which is decisive for system stability, is presented in Fig. 6c. The pressure drop evolution reveals two distinct regimes: an initial phase of linear increase, characteristic of a fully-developed, constant-property laminar flow, followed by a critical transition. The pivotal change occurs upon the flow entering the mushy zone. At this juncture, the pressure drop undergoes a sharp, nonlinear escalation. Such a drastic and accelerating increase in hydraulic resistance will inevitably trigger a consequential and severe attenuation of the bulk flow velocity. This attenuated velocity directly undermines the convective heat transport capacity, initiating a self-reinforcing (positive) feedback loop: reduced cooling capacity promotes further solidification, which in turn exacerbates the flow resistance, leading to even greater velocity decay. This closed-loop instability culminates in the irreversible and complete hydraulic blockage of the flow channel.

B. Dimensionless Analysis and Parametric Sensitivity

The theoretical analysis in the previous section indicates that a drop in molten salt temperature into the mushy zone

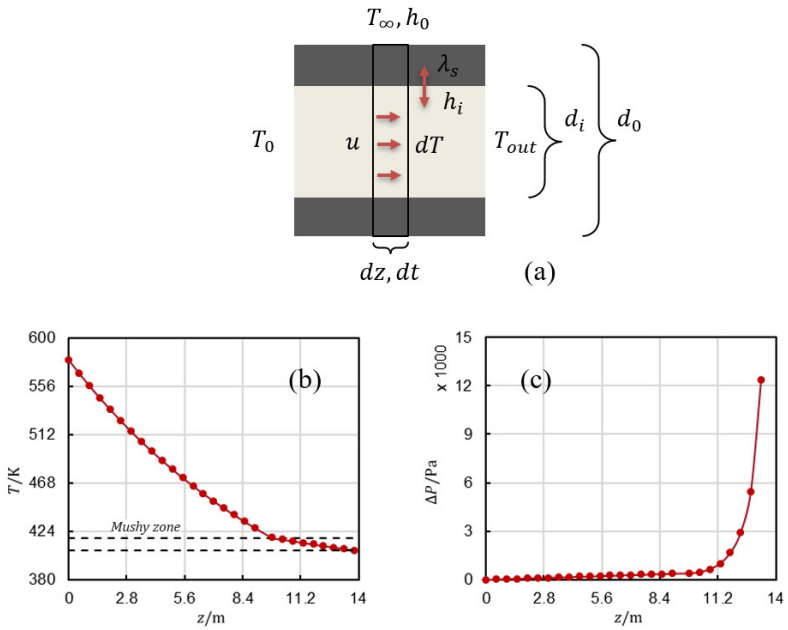

Fig. 6. (a) Schematic of the control volume and variations of flow parameters: (b) molten salt temperature (c) pressure drop.

leads to a sharp increase in pressure drop, readily resulting in flow blockage. A conservative design approach, therefore, prioritizes ensuring the fluid outlet temperature remains above this zone. Under this condition, the fluid temperature distribution follows Eq. (18), which can be expressed in a dimensionless form:

$$\theta = \frac{T_{out} - T_\infty}{T_l - T_\infty} = \frac{T_0 - T_\infty}{T_l - T_\infty} e^{-\frac{K}{\rho u c_l} \cdot \frac{A_1}{A_2}} \tag{26}$$

Here, T_{out} denotes the temperature at the pipe outlet ($z = l$), the heat transfer surface area is $A_1 = \pi d_o l$ and the fluid flow area is $A_2 = (1/4)\pi d_i^2$. Eq. (26) describes the cooling process of molten salt from a high inlet temperature towards the surrounding temperature, with the exponential decay term quantifying the cooling rate.

The onset of freezing risk occurs when the fluid temperature drops to the phase-change threshold, defined as $T = T_{freeze}$, signifying that heat dissipation has reached a critical level. The corresponding critical dimensionless temperature is:

$$\theta_{critical} = \frac{T_{freeze} - T_\infty}{T_l - T_\infty} \tag{27}$$

For Eq. (26), where $T_{freeze} = T_l$, we obtain $\theta_{critical} = 1$. A dimensionless temperature $\theta \leq 1$ indicates the fluid temperature has fallen below its liquid temperature, signaling a risk of freezing.

Based on Eq. (26), Fig. 7 reveals the sensitivity of the dimensionless temperature θ to various influencing parameters. The base case conditions for Hitec salt are: $T_0 = 435\,\mathrm{K}$, $u = 0.2\,\mathrm{m\,s^{-1}}$, $l = 3\,\mathrm{m}$, $T_\infty = 300\,\mathrm{K}$, $h_o = 20\,\mathrm{W\,m^{-2}\,K^{-1}}$, $h_i = 217\,\mathrm{W\,m^{-2}\,K^{-1}}$ (Nu = 4), $d_i = 10\,\mathrm{mm}$, and $d_t = 1\,\mathrm{mm}$. In the present study, the flow is laminar ($Re < 2000$) and the heat transfer is assumed to be under constant heat flux conditions. For fully developed laminar flow under constant heat flux, the theoretical Nusselt number is 4.36. The adoption of Nu = 4 is a simplification. It should also be noted that the Nusselt number here only evaluates the initial flow state. After the introduction of the mushy zone effect, the molten salt superficial velocity will change. The thermal conductivity of molten salt used to calculate h_i is evaluated at a reference temperature T_0 = 435 K. As illustrated in Fig. 7c, the sensitivity of h_i to the reference temperature is low under steady state conditions. The uncertainty introduced by these simplifications is small relative to other parameters uncertainties.

Fig. 7a illustrates the influence of flow velocity u and pipe length l. The dimensionless temperature exhibits a negative exponential relationship with the reciprocal of flow velocity. For $\theta > 1$, a steady flow equilibrium can always be established. However, when $u < 0.05\,\mathrm{m\,s^{-1}}$ leading to $\theta < 1$, flow oscillations will develop irreversibly towards freezing. For heat transfer pipes operating under low flow conditions, such as in natural circulation, the flow velocity is a critical parameter. Within a certain range, θ shows an approximately linear negative correlation with pipe length, indicating that excessively long heat exchanger tube bundles have a limited safe operating range for specific scenarios.

Fig. 7b shows the effects of inlet temperature T_0 and ambient temperature T_∞. The inlet temperature is the only variable demonstrating a significant positive correlation with θ, confirming that increasing the inlet temperature effectively reduces freezing risk. In contrast, the ambient temperature shows much lower sensitivity, with its positive correlation slope nearly 40 times smaller.

Fig. 7c presents the influence of the external and internal

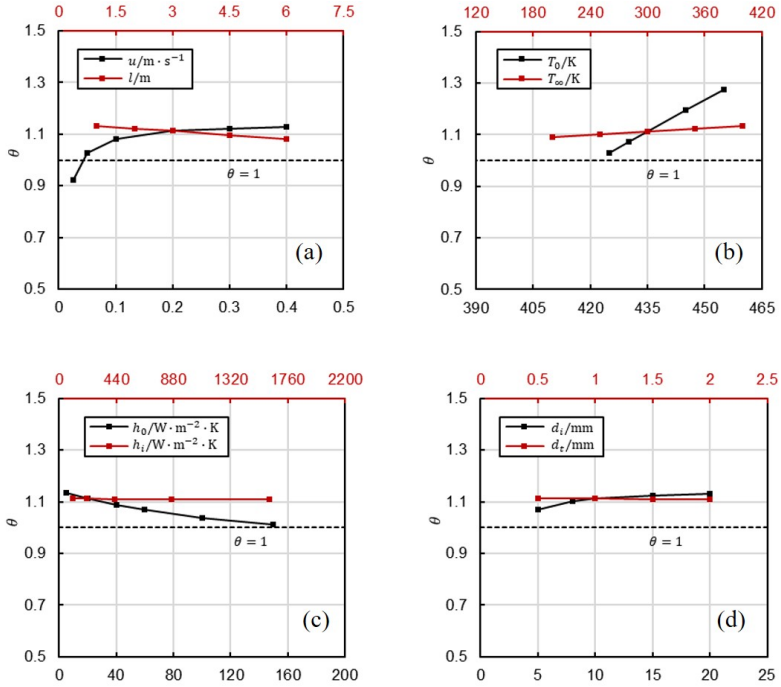

Fig. 7. Variation of the dimensionless temperature θ under different conditions. (a) u, l. (b) T_0, T_∞. (c) h_o, h_i. (d) d_i, d_t.

convection coefficients, h_o and h_i. Overall, θ has a negative exponential relationship with the external coefficient h_o. Within the plotted range, this appears nearly linear. When θ falls below 1, indicating freezing risk. This is particularly relevant for molten salt-to-air heat exchangers, where h_o is a practically adjustable parameter that must not be "over-conservatively" specified. The internal coefficient h_i, representing the Nusselt number (Nu), has an extremely low sensitivity on θ, implying that for $\theta > 1$, the internal heat transfer does not govern the final flow state.

Finally, Fig. 7d examines the impact of inner diameter d_i and pipe thickness d_t. For conventional pipe thicknesses (0.5 mm to 2 mm), the influence is negligible. Similar to flow velocity, a reduction in the inner diameter to 5 mm causes θ to begin following a distinct exponential decay. This observation reiterates a crucial design consideration: key heat exchange equipment in MSR decay heat removal systems, such as molten salt/air heat exchangers, often employ long, slender pipes operating for extended periods in environments below the salt's melting point. If such systems must adapt to special operating modes like natural circulation, the associated reduction in flow rate significantly increases freezing risk, making robust freeze-protection design paramount.

It should be acknowledged that, to the best of our knowledge, no existing experimental study can perfectly validate all aspects of the present conclusions. Nevertheless, partial validation using experimental data from a previous study (Fig. 2) confirms the feasibility and accuracy of the computational approach, particularly for the mushy zone constant. Recognizing the need for more rigorous validation, a comprehensive experimental campaign specifically designed for the present pipe geometry and flow conditions has been initiated, covering fluids from low melting point substitutes to actual high temperature molten salts, and the results will be summarized in future publications.

V. CONCLUSION

This study employs a multi-scale methodology, integrating a three-dimensional Computational Fluid Dynamics (CFD) model with a lumped-parameter model, to investigate the solidification and melting behaviors of molten salt during its flow into horizontal cold pipes. The key conclusions are summarized as follows:

- **Model verification: solidification-melting.** The system pressure balance calculation demonstrates that a mushy zone constant of $A_{mush} = 5 \times 10^4$ produces a simulated penetration distance in satisfactory agreement with the experimental results of Zhang et al. This calibrated parameter enables reliable calculation of the additional pressure drop within the Hitec salt mushy zone.

- **Filling dynamics and phase-change behavior of molten salt in a cold pipe.** The simulations depict the complete process from initial flow to final freezing. Under pressure-driven conditions, the flow velocity responds transiently to the increasing pressure drop caused by solidification. Two regimes are identified: i) Initial filling stage: Solidification initiates near

the cold wall. A minimum inlet temperature T_0 exists; below this value, the bulk salt temperature drops into the mushy zone during filling, leading to complete blockage. ii) Steady-state stage: A sudden increase in cooling causes colder fluid to settle at the pipe bottom under gravity, where solid accumulates. A critical external convection coefficient h_o is identified; when exceeded, the available pressure head cannot overcome the sharply rising flow resistance, resulting in irreversible flow decay and eventual freezing.

- **Extended model for temperature evolution and freeze-protection criterion.** Based on energy conservation, a model for temperature and pressure drop evolution is established. For the initial filling problem, the temperature profile aligns with the results of Zeng et al. Entry into the mushy zone induces a sharp pressure rise, indicating blockage risk. Therefore, a key design requirement is to keep the outlet temperature above the liquidus point. By defining a dimensionless temperature θ as the ratio of dissipated to inlet heat, the safety criterion is expressed as $\theta > 1$.

- **Parameter sensitivity ranking.** The expression of θ shows that blockage risk depends on the inlet temperature T_0, flow velocity, ambient temperature, internal and external convection coefficients (h_i, h_o), pipe diameter, and wall thickness. Under passive, low-velocity operation of a molten salt/air heat exchanger, the following sensitivity order is observed: increasing T_0 or reducing pipe length most significantly lowers risk; raising ambient temperature while reducing h_o is also effective; h_i and wall thickness exhibit low sensitivity.

Although the transient solidification phenomena predicted by the present CFD simulations, such as the location and evolution of the frozen salt plug, cannot be directly extrapolated from horizontal to vertical pipes due to gravity induced effects like particle settling and natural convection, the numerical methodology itself is fully applicable to vertical configurations. The same governing equations and the enthalpy porosity solidification model can be employed for vertical pipes by simply reorienting the gravitational vector. In contrast, the steady state heat transfer conclusions can be reasonably extrapolated to vertical pipes because the dominant heat transfer mechanisms in such cases are not affected by the direction of gravity. Nonetheless, dedicated validation for vertical geometries is recommended before quantitative application.

VI. NOMENCLATURE

A. General symbols

ΔP	pressure drop [Pa]
ΔP_f	frictional pressure drop [Pa]
ΔP_e	additional pressure drop [Pa]
f	friction factor [-]
l	pipe length [m]
d_i	pipe inner diameter [mm]
d_o	pipe outer diameter [mm]
d_t	pipe thickness [mm]
u	velocity [m·s^{-1}]
$\vec{v}$	velocity vector [m·s^{-1}]
Re	Reynolds number [-]
Nu	Nusselt number [-]
R_1	inner pipe radius [m]
R_2	outer pipe radius [m]
T	temperature [K]
T_p	initial pipe temperature [K]
T_i	characteristic temperature [K]
T_∞	surrounding temperature [K]
t	time [s]
A_{mush}	mushy zone constant [-]
f_l	liquid fraction [-]
g	acceleration of gravity [m·s^{-2}]
Q	latent heat of fusion [kJ·kg^{-1}]
c	specific heat capacity [J·kg^{-1}·K^{-1}]
h_i	convective heat transfer coefficient in the pipe [W·m^{-2}·K^{-1}]
h_o	convective heat transfer coefficient out the pipe [W·m^{-2}·K^{-1}]

B. Greek symbols

ρ	density [kg·m^{-3}]
σ	surface tension [N·m^{-1}]
μ	dynamic viscosity [Pa·s]
λ	thermal conductivity [W·m^{-1}·K^{-1}]

C. Subscripts

0	initial condition
in	inlet pipe
c	cold pipe
m	molten salt
l	liquid
s	solid
w	wall
a	air
st	steel

[1] G.J. Janz, Molten Salts Handbook. Academic Publisher, New York (1967) doi: 10.1016/B978-0-123-95642-2.X5001-1

[2] Xu H.J., Dai Z.M., Cai X.Z. et al. Thorium-based molten salt reactor and comprehensive utilization of nuclear energy. Modern Physics. **30**(4), 25–34 (2019). doi: 10.13405/j.cnki.xdwz.2018.04.007

[3] Jérôme S., Michel A., Ondřej B. et al., The molten salt reactor (MSR) in generation IV: Overview and perspectives. Prog. Nuclear Energy. **77**, 308–319 (2014). doi: 10.1016/j.pnucene.2014.02.014

[4] Zhimin Dai, 17 - Thorium molten salt reactor nuclear energy system (TMSR). Editor(s): Thomas J. Dolan. Molten Salt Reactors and Thorium Energy, Woodhead Publishing, 531–540 (2017). doi: 10.1016/B978-0-08-101126-3.00017-8

[5] Y.F. Liu, R. Yan, Y. Zou et al., Sensitivity/uncertainty comparison and similarity analysis between TMSR-LF1 and MSR models. Prog. Nuclear Energy. **122**, 103289 (2020). doi: 10.1016/j.pnucene.2020.103289

[6] M.D. Mei, X.W. Chen, S.D. Sun et al., Design and flow field analysis for visualization experiment facility of pebble bed based on molten salt reactor. Nucl. Sci. Tech. **30**(3), 51 (2019). doi: 10.1007/s41365-019-0574-6

[7] D.L. Zang, S.Z. Qiu C.L. Liu et al., Steady thermal hydraulic analysis for a molten salt reactor. Nucl. Sci. Tech. **19(3)**, 187–192 (2017). doi: 10.1016/S1001-8042(08)60048-2

[8] R.M Ji, Y. Dai, G.F. Zhu et al., Evaluation of the fraction of delayed photoneutrons for TMSR-SF1. Nucl. Sci. Tech. **28(9)**, (2017). doi: 10.1007/s41365-017-0285-9

[9] C.Y. Zou, C.Z. Cai, C.G. Yu et al., Transition to thorium fuel cycle for TMSR. Nucl. Eng. Des. **330**, 420–428 (2018). doi: 10.1016/j.nucengdes.2018.01.033

[10] Y. Wang, J. Tian, S.W. Wang et al., Experimental study on the penetration characteristics of leaking molten salt in the thermal insulation layer of aluminum silicate fiber. Nucl. Sci. Tech. **32**, 92 (2021). doi: 10.1007/s41365-021-00935-6

[11] E.L. Meng, T. Xia, D.L. Zhang, Experimental study of the thermal and power generation performance of a new type of water-cooling photovoltaic/thermal system. Appl. Therm. Eng. **286**, 129352 (2026). doi: 10.1016/j.applthermaleng.2025.129352

[12] J.C Zhuang, J. Chen, B.J. Wei et al., Recent advances in chloride molten salt-based thermal energy storage: Melting behavior, modification, and corrosion mitigation strategies. Renew Sustain Energy Rev. **229**, 116639 (2026). doi: 10.1016/j.rser.2025.116639

[13] Y. T, M. K, I. K et al., Transient Response of Small Molten Salt Reactor at Duct Blockage Accident. Trans. JSME, B **71**, 2537–2544 (2005). doi: 10.1299/kikaib.71.2537

[14] R.M. W, K.P. R, B.R. B, Molten-Salt Reactors—History, Status, and Potential. Nucl. Appl. Tech. **8(2)**, 107–117 (1970). doi: 10.13182/NT70-A28619

[15] P.Y. Huang, C. Zhou, S.Y. Xue et al., Extension and application of liquid fuel molten salt reactor system analysis program based on ATHLET 3.2 program. Ann. Nucl. Energy. **221**, 111522 (2025). doi: 10.1016/j.anucene.2025.111522

[16] Xu, B., Zou, Y., Sun, Q. et al., Accident analyses of station blackout for TMSR-SF2. Nucl. Tech. 40 **44**, 57–62 (2017). doi: 10.11889/j.0253-3219.2017.hjs.40.100601

[17] K. Wang, C.Q. Wang, Q. Yang et al., Uncertainty and sensibility analysis of loss-of-forced-cooling accidents for 150-MWt Molten Salt Reactors. Nucl. Sci. Tech. **36**(6), 111 (2025). doi: 10.1007/s41365-025-01681-9

[18] N. Le Brun, G.F. Hewitt, C.N. Markides, Transient freezing of molten salts in pipe-flow systems: Application to the direct reactor auxiliary cooling system (DRACS). ApEn. **186**(1), 56–67 (2017). doi: 10.1016/j.apenergy.2016.09.099

[19] APPENDIX B - Direct reactor auxiliary cooling system (DRACS). Editor(s): Bahman Zohuri. Molten Salt Reactors and Integrated Molten Salt Reactors, Academic Press. 253–262 (2021). doi: 10.1016/B978-0-323-90638-8.00009-6

[20] S.Y. Xue, C. Zhou, P.Y. Huang et al., Review of conceptual design and fundamental research related to the passive residual heat removal system in molten salt reactors. Nucl. Eng. Des. **442**, 114275 (2025). doi: 10.1016/j.nucengdes.2025.114275

[21] C. Zeng, X. Chu, L.M. Liu et al., Performance evaluation of DRACS system of molten salt reactors using a transient solidification model. Nucl. Eng. Des. **386**, 111565 (2022). doi: 10.1016/j.nucengdes.2021.111565

[22] Ji C., Qin Z., Dubey S. et al., Simulation on PCM melting enhancement with double-fin length arrangements in a rectangular enclosure induced by natural convection. Int. J. Heat Mass Transf. **127**, 255–265 (2018). doi: 10.1016/j.ijheatmasstransfer.2018.07.118

[23] Jiang D., Liao Z., Li P. et al., The evolution of the mushy zone during the melting process of a binary nitrate salt. Int. J. Heat Mass Transf. **142**, 118456 (2019). doi: 10.1016/j.ijheatmasstransfer.2019.118456

[24] Pal D., Joshi Yogendra K., Melting in a side heated tall enclosure by a uniformly dissipating heat source. Int. J. Heat Mass Transf. **44**, 375–387 (2001). doi: 10.1016/S0017-9310(00)00116-2

[25] Jun K., Sukeharu N., Masahiro K. et al., Effect of mushy zone constant in Voller-Prakash model on keyholing behaviour in laser powder bed fusion simulation. Results Eng. **24**, 103567 (2024). doi: 10.1016/j.rineng.2024.103567

[26] J.E. Pacheco, M.E. Ralph, J.M. Chavez, Investigation of cold filling receiver panels and piping in molten-nitrate-salt central-receiver solar power plants. J. Solar Energy Eng. Trans. ASME. **117**, 282–289 (1995) doi: 10.1115/1.2847839

[27] D. Bestion, 11 - The structure of system thermal-hydraulic code for nuclear reactor applications. Editor(s): F. D'Auria, Y. A. Hassan, In Woodhead Publishing Series in Energy, Handbook on Thermal Hydraulics in Water-Cooled Nuclear Reactors (Second Edition), Woodhead Publishing, 71-249 (2024). doi: 10.1016/B978-0-323-85610-2.00019-3

[28] Lu J.F., Ding J., Filling dynamics and phase change of molten salt in cold receiver pipe during initial pumping process. Int. J. Heat Mass Transf. **64**, 98–107 (2013). doi:10.1016/j.ijheatmasstransfer.2013.04.021

[29] Yu H.X., Zhou C., Yuan X.F. et al., Study on solidification behaviors and pressure drop characteristics of molten salt in filling cold pipe. Ann. Nucl. Energy. **225**, 111794 (2025). doi:10.1016/j.anucene.2025.111794

[30] Jansson N., Karp M., Podobas A. et al., Neko: A modern, portable, and scalable framework for high-fidelity computational fluid dynamics. Comput. Fluids. **275**, 106243 (2024). doi:10.1016/j.compfluid.2024.106243

[31] Mahmut C.K., Tomas K., Jan S. et al., Numerical and experimental investigation of melting and solidification of molten salt in freeze valve. Appl. Therm. Eng. **269**, 126206 (2025). doi:10.1016/j.applthermaleng.2025.126206

[32] Fausto D., Konstantinos G., Lucia P. et al., Integration of multi-fidelity methods in parametrized non-intrusive reduced order models for industrial applications. J. Comput. Sci. **85**, 102511 (2024). doi:10.1016/j.jocs.2024.102511

[33] Wu H.B., Wang X.J., Su W. et al., Machine Learning-based Reduced-Order Model and multi-fidelity approaches for field reconstruction in CFD: A review. Chem. Eng. Sci. **322**, 123156 (2025). doi:10.1016/j.ces.2025.123156

[34] C. Zeng, C. Shen, M.L. Liu et al., Development of a solidification blockage discriminant model in filling pipelines. Ann. Nucl. Energy. **206**, 110669 (2024). doi: 10.1016/j.anucene.2024.110669

[35] Zhang W.H., Liu M.L., Zeng C. et al., Experimental and numerical simulation study on the solidification behavior of molten salt reactor coolants. Nucl. Tech. **48**(4), 040603 (2025). doi: 10.11889/j.0253-3219.2025.hjs.48.230405

[36] J.H. Lienhard IV, J.H. Lienhard V, A Heat Transfer Textbook. Phlogiston Press, Cambridge, Massachusetts, USA (2002)

[37] R. Scardovelli, S. Zaleski, Direct numerical simulation of free-surface and interfacial flow. Annu. Rev. Fluid Mech. **31**, 567–603 (1999). doi: 10.1146/annurev.fluid.31.1.567

[38] Hirt C.W., Nichols B.D., Volume of fluid (VOF) method for the dynamics of free boundaries. J. Comput. Phys. **39**, 201–225 (1981). doi: 10.1016/0021-9991(81)90145-5

[39] Voller V.R., Prakash C., A fixed grid numerical modelling methodology for convection-diffusion mushy region phase-change problems. Int. J. Heat Mass Transf. **39(8)**, 1709–1719 (1987). doi: 10.1016/0017-9310(87)90317-6

[40] Brent A.D., Voller V.R., Reid K.J., Enthalpy-porosity technique for modeling convection-diffusion phase change: application to the melting of a pure metal. Num. Heat Transf. Part B. **13(3)**, 297–318 (1988). doi: 10.1080/10407788808913615

[41] Voller V.R., Markatos N.C., M. Cross, Solidification in convection and diffusion. In: Markatos N.C., Tatchell D.G., Cross M., Rhodes N. (eds) Numerical Simulations of Fluid Flow and Heat/Mass Transfer Processes, pp. 425–432. Springer, Berlin (1986) doi: 10.1007/978-3-642-82781-5_33

[42] Carman, P.C., Fluid flow through granular beds. Trans. Inst. Chem. Engrs **15**, 150–156 (1937) doi: 10.1016/S0263-8762(97)80003-2

[43] H.X. Yu, C. Zhou, X.F. Yuan et al., Influence of mushy zone constant on solid-liquid phase change behaviors and characteristics of molten salt in filling process. Nucl. Sci. Tech. **48(7)**, 070023 (2025). doi: 10.11889/j.0253-3219.2025.hjs.48.240306